NORTHERN ILLINOIS UNIVERSITY

Chert formation at IODP Site U1521 as a proxy for variations in marine
geochemistry at the onset of the Miocene Climate Optimum

A Capstone Submitted to the
University Honors Program
In Partial Fulfillment of the
Requirements of the Baccalaureate Degree
With Honors

Department Of

Geology and Environmental Geosciences

By

Finlay McElmeel

DeKalb, Illinois

December 2021

University Honors Program
Capstone Faculty Approval Page

Capstone Title (print or type)

Chert formation at IODP Site U1521 as a proxy for variations in marine

geochemistry at the onset of the Miocene Climate Optimum

Student Name (print or type) _____ Finlay McElmeel _____

Faculty Supervisor (print or type) ____ Dr. Justin Dodd _____

Faculty Approval Signature _____ *[signature: Justin Dodd]* _____

Department of (print or type) _____ Department of Geology and Environmental Geosciences ____

Date of Approval (print or type) ____ December 3, 2021 _____

Date and Venue of Presentation ____ November 5, 2021: Department Colloquium _____

Check if any of the following apply, and please tell us where and how it was published:

☐ Capstone has been published (Journal/Outlet):

_____

☐ Capstone has been submitted for publication (Journal/Outlet):

_____

Completed Honors Capstone projects may be used for student reference purposes, both electronically and in the Honors Capstone Library (CLB 110).

If you would like to opt out and not have this student's completed capstone used for reference purposes, please initial here: _____ (Faculty Supervisor)

Chert formation at IODP Site U1521 as a proxy for variations in marine geochemistry at the onset of the Miocene Climate Optimum

Abstract

The goal of International Ocean Discovery Program (IODP) Expedition 374 in the Ross Sea, Antarctica was to collect marine sediment drill cores that would demonstrate the changes in the Antarctic Ice Sheets mass balance during times of Earth history when global temperatures and atmospheric CO_2 were higher than today. Intervals such as the Miocene Climatic Optimum (MCO; ~17-14.5 million years ago) provide insights into what a future world could look like (Shevenell et al., 2004; Levy et al., 2016). Ice-proximal records from the near-Antarctic coast, such as those collected during IODP Exp 374, may hold critical information to understanding far-reaching impacts of the Antarctic Ice Sheets on global environmental changes. Depositional reconstructions of past glacial and open marine conditions in the region provide environmental constraints used to model changes in the Antarctic Ice Sheets. In my study, I will explore the presence of glacial deposits (till delta features), which prograde onto stratified glaciomarine sediment in several locations in the region during the Early to Middle Miocene (17.6-16.9 million years ago), immediately preceding the MCO. The samples presented here were collected from IODP Exp 374 Site U1521, from a depth of 287.21 to 344.92 meters below the sea floor (mbsf) and made up of a dark grey, massive to stratified diatom-bearing and clast-poor sandy diamictite as well as grey chert nodules interbedded with dark grey, silica cemented, faintly irregularly laminated mudstones (McKay et al., 2019). This study supports the basic shipboard lithological data, but there is distinct variability in the silica-carbonate content of the chert and upper diamictite layers. These data provide additional evidence for a significant change in

depositional environment as a result of fluctuations in the in the Ross Ice Shelf that predate the MCO.

Background

Recent climate change has resulted in alterations in the Antarctic Ice Sheets, the long-term consequences of which are not entirely understood at present. What is known is that the polar ice sheet mass balance does have an impact on global sea level and circulation. While there is no direct analogue to present conditions, there are intervals in geologic history, such as the Miocene Climatic Optimum (MCO; ~17-14.5 million years ago), that were approximately 4°C warmer than present day. Current predictions of climate change put the increase of average global temperature at or near MCO temperatures by the year 2100 if there is no change in global CO_2 emissions (IPCC, 2021). As a result, past variations in the Antarctic Ice Sheets could hold vital information for understanding their future contributions to future sea level and climate changes (McKay et al., 2019).

The primary goals of International Ocean Discovery Program (IODP) Expedition 374 were to collect marine sediment cores along a transect from the outer continental shelf to rise in the Ross Sea, Antarctica to develop records of ice-sheet variability from the Miocene through the Pleistocene. Existing models have demonstrated the region is sensitive to changes in ocean heat flux and are thus ideal to reconstructing climate forcings and feedbacks associated with Antarctic ice mass fluctuations (McKay et al., 2019).

Previous records suggest that during the early Miocene, a temporary and sudden increase in ice volume occurred as a result of orbital forcing and a decrease in atmospheric CO_2 content. Benthic foraminifera oxygen isotope records and other marine sediment data suggest that the orbital influences of obliquity (~40-kyr) and eccentricity (~100-kyr) are responsible for cyclic

nature of the East Antarctic margin (Naish et al., 2008; 2009). The onset of these orbital

parameters is poorly constrained; however, multiple records have suggested that the link between

the orbital cycles and the extent of the East Antarctic Ice Sheet was in place at the

Oligocene/Miocene transition (~23 million years ago; e.g., Naish et al., 2001). Additionally, the

atmospheric CO_2 content fell from 1000 to 1500 ppm to ~650 ppm from the Eocene to

Oligocene. The CO_2 content continued to fall to ~400 ppm during the early Miocene; however,

far-field marine sediment records suggest there was little growth or retreat of continental ice

sheets after the East Antarctic Ice Sheet's "capacity" had been reached (Pagani et al., 2005;

Foster and Rohling, 2013). The increase in temperature corresponding to the MCO resulted in

significant portions of the ice sheets melting, increasing sea levels anywhere from 20 m to 60 m

(Miller et al., 2005; 2012 Kominz et al., 2008; Naish and Wilson, 2009; John et al., 2011), which

is in direct conflict with records suggesting the Antarctic ice sheets remained relatively stable

through this time.

The Middle Miocene Climate Transition (MMCT; ~14.2-13.8 million years ago) marks

the first known evidence of the expansion and growth of the West Antarctic Ice Sheet, indicated

by glacial unconformities at the Ross Sea outer continental shelf. The exact timing of the event,

however, is not well constrained (Bart, 2003; McKay et al., 2019; Marschalek et al., 2021), and

far-field evidence suggests the growth may have begun sooner than the MMCT (Shevenell et al.,

2004; 2008).

The evidence of 20 to 60 m sea level fluctuations during the MCO suggests near-

complete loss of the East Antarctic Ice Sheet to compensate for the change, but this is

incompatible with current models of the East Antarctic Ice Sheet (Pekar and DeConto, 2006;

Kominz et al., 2016; Miller et al., 2020). Substantial loss of the West Ice Sheet, however, could

explain sea level variation, and evidence for collapse of the ice sheet at the last interglacial period ~125,000 years ago (Scherer et al., 1998; Kopp et al., 2009; Naish et al., 2009; McKay et al., 2012) supports the possibility. Depositional reconstructions of past conditions can help constrain if a substantial West Antarctic Ice Sheet could be supported prior to the MMCT and into the MCO. If the West Antarctic Ice Sheet could be supported during significantly warmer periods of time in Earth's past, it could provide insight into the consequences anthropogenic climate change.

Geologic Setting

The Middle Jurassic initiation of the West Antarctic Rift led to the breakup of Gondwana, the opening of the Ross Sea (Behrendt et al., 1991), and the subsequent development of its three sedimentary basins (Cooper et al., 1991). The majority of past drilling operations have focused on the Victoria Land Basin, the furthest west of the three, while Exp 374 focused mostly on the Eastern Basin of the Ross Sea (Fig. 1). The region's basement is comprised mostly of high-grade metamorphic and calcareous rocks which have been heavily fractured and recrystallized as mylonite through the Late Cretaceous uplift (Siddoway et al., 2004). There is no evidence of basement rock younger than Devonian, suggesting the Ross Sea was likely a region of uplift and erosion for most of the Permian to Triassic (Barret, 1981). Eight seismic units have been defined in the sediment infill (RSS-1 to RSS-8), bounded by six major shelf-wide unconformities (RSU 1-6; De Santis et al., 1995; McKay et al., 2019). Nearby deep-water basins in the outer Ross Sea have remained free of grounded ice up to the late Oligocene, but progressive shoaling in the Eastern Basin provides evidence of what was likely sediment-filled meltwater plumes paired with temperate glacial sedimentation (De Santis, 1995). RSU4, a primary target of Site U1521, implies a shelf-wide advance of grounded marine-based ice sourced from the East Antarctic Ice

Sheet during the MMCT, and is the first indisputable evidence of a glacially carved trough in the

Ross Sea (De Santis, 1995; Ten Brink et al., 1995; Passchier et al., 2011; Levy et al., 2016;
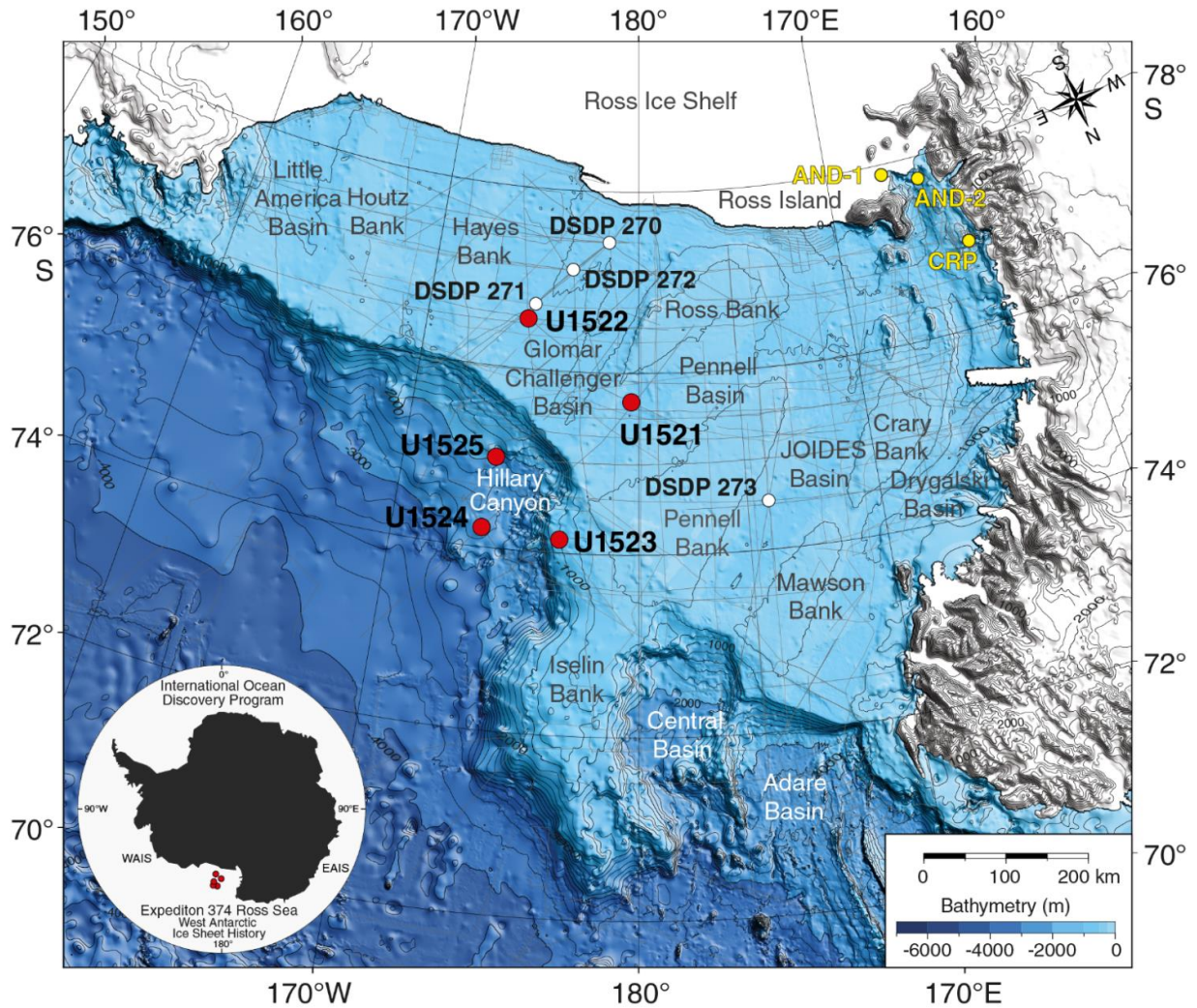
Anderson et al., 2018).

Figure 1: A bathymetric map of IODP Expedition 374 sites (red), and previous drill sites from

DSDP Leg 28 (white), CRP, and AND sites (yellow) (McKay et al., 2019).

Site Summary

 IODP Site U1521 is located on the mid-to-outer continental shelf in the Pennell Basin at a water depth of 562 m. The primary purpose of the site was to collect sedimentary data above and below RSU4, interpreted to be the result of cross-shelf expansion of the East Antarctic Ice Sheet during the Miocene (McKay et al., 2019).

 Initial coring at Site U1521 called for rotary core barrel (RCB) drilling to 950 mbsf, though actual depth drilled was 650.1 mbsf. Through to Core 37R, collection proceeded without incident, though Cores 32R to 37R saw a significant drop in recovery as the interval was comprised of harder clasts that clogged the core barrel. From Cores 37R to 43R, half-length cores were collected, increasing recovery once again, before returning to full length cores from Core 44R to 71R, after which drilling was terminated (McKay et al., 2019).

 Cores collected from Site U1521 were classified into seven lithostratigraphic units (I-VII), youngest to oldest, with Unit VI being broken into three subunits (VIA-VIC, youngest to oldest; Fig. 2). RSU4 lies between Units IV and V (McKay et al., 2019).
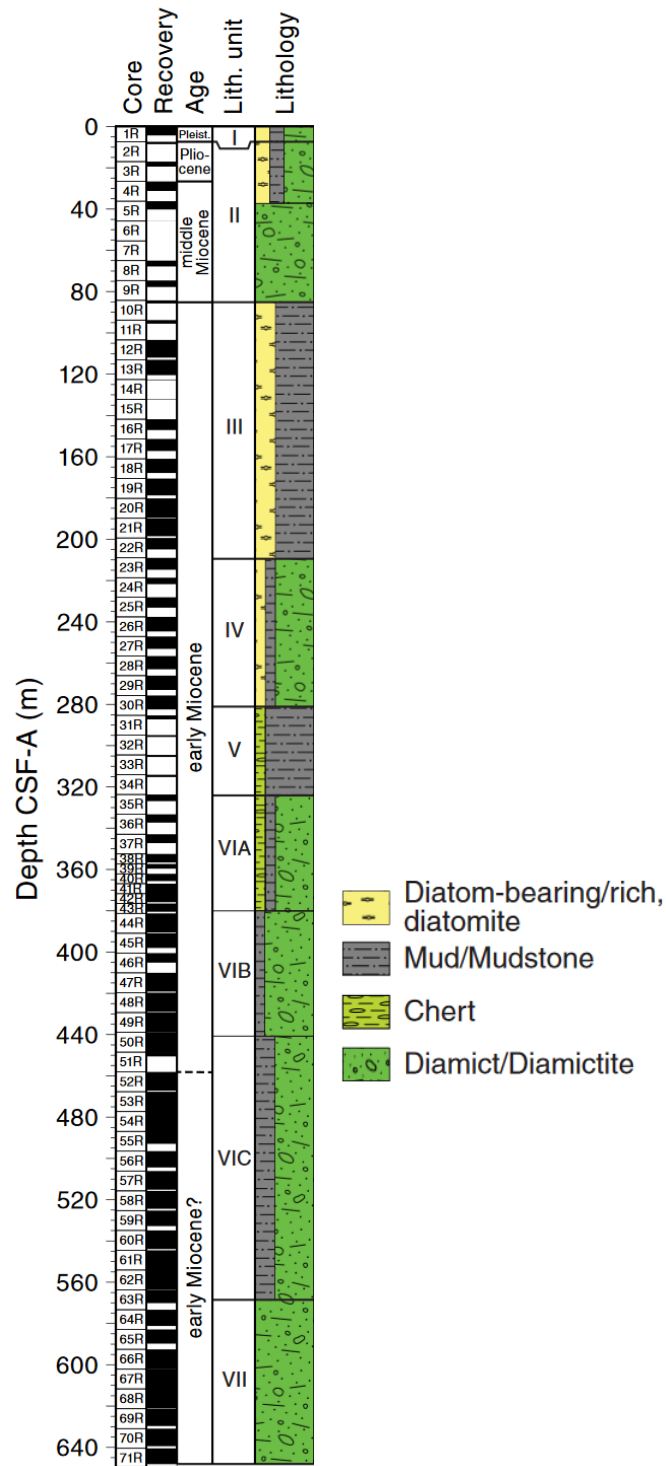
Figure 2: A stratigraphic column of Site U1521, containing core number, recovery, relative age, lithologic unit, and lithology (adapted from McKay et al., 2019).

Unit I (0-7.40 mbsf) consists of olive to light olive gray unconsolidated diatom-rich mud to a dark grayish brown diatom-bearing mud, with two intervals of a gray sandy, diatom-bearing mud and dispersed clasts throughout. Recovery in the unit was 58% (McKay et al., 2019).

Unit II (7.40-85.34 mbsf) is made of interbedded, dark gray lithified and massive clast-poor sandy diamictite, muddy diatomite, and diatom-bearing to rich mudstone (McKay et al., 2019). The diamictite beds were up to ~6 m thick and massive, with subangular to rounded clasts of varying compositions were randomly distributed throughout. The remaining two rock types were on a centimeter to decimeter scale, heavily bioturbated, and contained dispersed clasts, mud clasts, and shell fragments. The recovery of the unit was 25% (McKay et al., 2019).

Unit III (85.34-209.17 mbsf) comprises of an olive gray to greenish gray, moderately to highly bioturbated diatom-bearing to rich mudstone. Pyrite staining, faint laminations were seen throughout, as well as carbonate cemented intervals. Recovery through the unit was 55% (McKay et al., 2019).

Unit IV (209.17-280.72 mbsf) is made of a dark gray massive to stratified diatom-bearing and clast-poor sandy diamictite, with centimeter to decimeter scale interbedded mudstone and diamictite at the top of the unit. The diamictite has a widely varying clast composition, while mud clasts, foraminifera, and shell fragments, sometimes with associated carbonate concretions, are distributed randomly throughout the unit as well. The unit recovery was 63% (McKay et al., 2019).

Unit V (280.72-324.20 mbsf) is made of gray chert nodules with interbedded dark-gray silica cemented mudstones, with faint irregular laminae in the mudstone. Most cores recovered in the unit comprise of chert nodules that clogged the core barrel and drastically reduced recovery (McKay et al., 2019).

Unit VI (324.20-567.95 mbsf) is primarily interbedded diamictite and mudstone, divided into different subunits based on the observed interbedding. Subunit VIA (324.20-380.04 mbsf) consists of interbedded very dark gray to gray, massive, clast-rich and sandy to clast-poor and muddy diamictite, and dark greenish-gray mudstone. Recovery of Subunit VIA was 60%. Subunit VIB (380.04-440.58 mbsf) is a very dark gray to dark greenish gray, massive to stratified, clast-rich to poor sandy diamictite. Shell fragments, foraminifera, a faint vein network, and carbonate nodules/concretions are present throughout the subunit. Recovery was 85%. Subunit VIC (440.58-567.95 mbsf) is interbedded clast-poor diamictite and very dark greenish gray mudstone, containing faint vein networks, large clasts, shell fragments, and carbonate concretions. Recovery of this subunit was 88% (McKay et al., 2019).

Unit VII (567.95-648.17 mbsf), the oldest of the cored units, consists of interbedded, very dark greenish gray clast-poor sandy to clast-rich muddy diamictite. Intervals of the unit have fine wavy laminations and slight stratification, while carbonate concretions, shell fragments, faint vein networks, and clasts of varying size are present throughout the unit. Recovery in the unit was 86% (McKay et al., 2019)

The samples I discuss here are from Units V and VIA, where intervals of chert formation resulted in poor recovery and limited samples. Samples 31RCCW, 33R1W, and 34RCCW are chert nodules from Unit V. Samples 36R1W, 37R2W 15-17, and 37R2W 65-67 are all from Unit VIA and represent the transition to diamictite.

Methods

Sample Collection

Cores 32R to 37R suffered from a significant drop in recovery (25%) as a result of hard clasts clogging the core barrel and merely pushing through the softer material. Half-length cores

of 4.8 m, as opposed to 9.6 m, were collected for Cores 38R to 43R (352.5-381.3 mbsf), substantially improving recovery of the intervals (80%). 9.6 m cores with the initial RCB core system were collected for Cores 44R to 71R (381.3-650.1 mbsf) after the material became less indurated. Coring ended at 650.1 mbsf as the primary scientific objectives of the site had been met. Overall, 411.50 m of core were recovered (63%) (McKay et al., 2019).

Sample Selection

Sub-samples of lithified core sediments (e.g., chert and diamictite) were collected at the Gulf Coast Repository using a rock saw. Six samples were selected from Site U1521 for this study. Samples 31RCCW, 33R1W, and 34RCCW were selected as representative samples of the poorly recovered chert interval, while samples 36R1W, 37R2W (15/17), and 37R2W (65/67) were selected as representative of the diamictite interval (Table 1; Fig. 3).

Table 1: Summary of the samples used in this study; the core number, interval, depth of the sample, what unit it was initially identified as, a brief description, and the relative age of the samples.

Core	Interval	Depth CSF-A (m)	Unit	Basic Unit Description	Age
31RCCW	8/10	287.12	V	Chert nodules and mudstone	Early Miocene
33R1W	30/32	304.80	V		
34RCCW	13/15	315.08	V		
36R1W	35/37	333.65	VIA	Interbedded mudstone and diamictite with silica cementing	
37R2W	15/17	344.42	VIA		
37R2W	65/67	344.92	VIA		
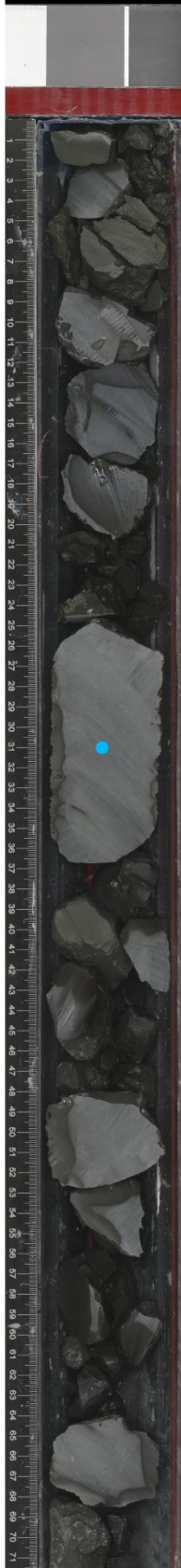
Figure 3: Core images taken shipboard during IODP Expedition 374. Samples from this study are taken from the intervals marked by the blue dots and are discussed using the corresponding core number (an exception is made for Core 37R; two different samples are referred to with the interval as well to differentiate).

Preparing Billets

Samples were cut down to size in order to fit on 1 cm by 5 cm frosted glass slides. The cut sides were sanded smooth to affix them to the slides using a carbon-based epoxy. The epoxy was left to cure for two days, and once cured, the excess sample was cut down to a thick section billet 2 mm thick. The freshly cut side was then polished smooth in the same fashion as before to prepare them for coating before going into the SEM. After sanding, the samples were scanned to get high quality images for later reference.

SEM/EDS

The billets were thinly coated with a gold layer 0.05 µm thick using a Polaron SEM Coating System for 60 seconds at 2.5 kV. Once coated, each sample was placed in a JEOL JSM-5610LV Scanning Electron Microscope (SEM). Each sample was imaged for any notable features using backscatter imaging at a working distance of 15 mm, a 20 kV beam, and 1 µm scale. The high-quality images captured before coating were used as reference maps of the samples. The Energy Dispersive X-ray Analysis (EDS) functions of the SEM were used to collect bulk mapping data. Weight percent, atomic percent, percent errors for each, and images were collected at numerous sites on each sample. An elemental and phase map, and the corresponding spectra, were collected at locations considered to be representative of the bulk sample for each sample as well.

LA-ICP-MS

After SEM analysis, the samples were removed, and locations of interest from the collected EDS data were mapped on the samples, and on printed versions of the pre-coated sample scans. Each sample was ablated using a Thermo-Fisher Scientific Element 2 Inductively Coupled Plasma Mass Spectrometer (ICP-MS) equipped with a Teledyne-Photon-Machines

Analyte G2 laser ablation system. The instrumentation was set to a laser frequency of 10 Hz, a fluence of ~7.7 J/cm^2, and beam size of 135 microns over 60 seconds. Elements of interest were ^{23}Na, ^{25}Mg, ^{27}Al, ^{29}Si, ^{34}S, ^{35}Cl, ^{39}K, ^{43}Ca, ^{47}Ti, ^{55}Mn, ^{57}Fe, ^{88}Sr, ^{146}Nd, and ^{238}U. These isotopes were used for consistency, but they were not quantified over the analysis. Exact results were dependent on tuning, carried out using a NIST-612 standard to monitor both stability and intensity of ^{45}Sc, ^{115}In, ^{238}U, low rates of UO/U, and of $^{137}Ba^{2+}/^{137}Ba^{+}$. External calibrations were conducted using NIST-612, NIST-610, GSE-1G, BHVO-2G, BIR-1G, and BCR-2G standards (Jochum et al., 2015). Analyses were completed in two overall runs, with the ICP-MS in hot plasma mode and isotope measurements collected in low resolution mode.

^{29}Si was used as the internal standard for most samples, with the values determined by sample-averaged matrix-analyses collected from the EDS data. All major elemental data was assumed and normalized to a theoretical sum of 100% oxides, and the same was assumed for trace element data. The only exception to this was 36R1W 35/37, which had ^{25}Mg and ^{43}Ca assumed as $MgCO_3$ and $CaCO_3$ respectively, as suggested by EDS data. The remaining diamictite samples, 37R2W 15/17 and 37R2W 65/67, where primarily composed of a carbonate matrix (primarily calcite, though some dolomite was present), with the exact carbonate rations unable to be determined on the ICP-MS. The data collected from the two samples were calibrated using the ^{29}Si internal standard and are thus more qualitative.

Results

SEM/EDS

<u>31RCCW</u>

EDS analysis presented a uniform microcrystalline matrix of silicates, high in SiO_2. There was evidence of pyritized organic material throughout, with the individual framboids

visible in many cases. Individual foraminifera with calcite shells, infilled with the same silica matrix, were scattered throughout, though the individual species were outside the scope of the project (Fig. 4)

<u>33R1W</u>

The sample was similar to 31RCCW, with a matrix high in SiO_2 and other silicates. There are few individual crystals, though clay minerals, isolated feldspars clasts, and more pyritized matter are present in places. Several more calcite foraminifera shells are present as well (Fig. 5).

<u>34RCCW</u>

34RCCW was the last of the samples with a microcrystalline silicate matrix, high in SiO_2. Clay minerals, felspar clasts, and pyritized organic material were all present. Clasts were slightly larger than previous samples and were more distinct, though they remained isolated. The first evidence of opal-CT was seen in this sample as well (Fig. 6).

<u>36R1W</u>

This sample was the first of the three diamictites and comparatively clast poor in regard to the other two. The matrix was initially identified as carbonate, with clasts of K, Na, Ca-feldspars, more of the pyritized matter (including pyritized diatoms), and calcite-shelled foraminifera and diatoms present (Fig. 7).

<u>37R2W 15/17 and 37R2W 65/67</u>

Sample 37R2W 15/17 was the first of the clast heavy diamictites, with similar clast composition as 36R1W, with the additional presence of quartz clasts. There is further evidence of opal-CT, present in small crevices in the sample. Sample 37R2W 65/67 had the same broad composition, with a lower density of clasts. Those that were present had the same composition as

those in 37R2W 15/17, though there was rare incorporation of other materials such as
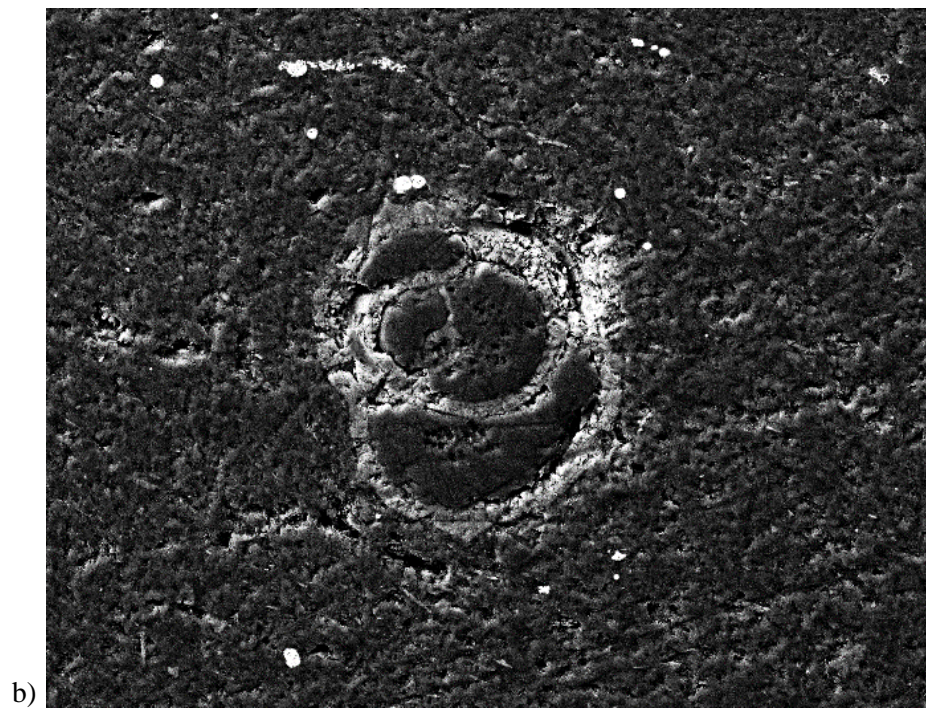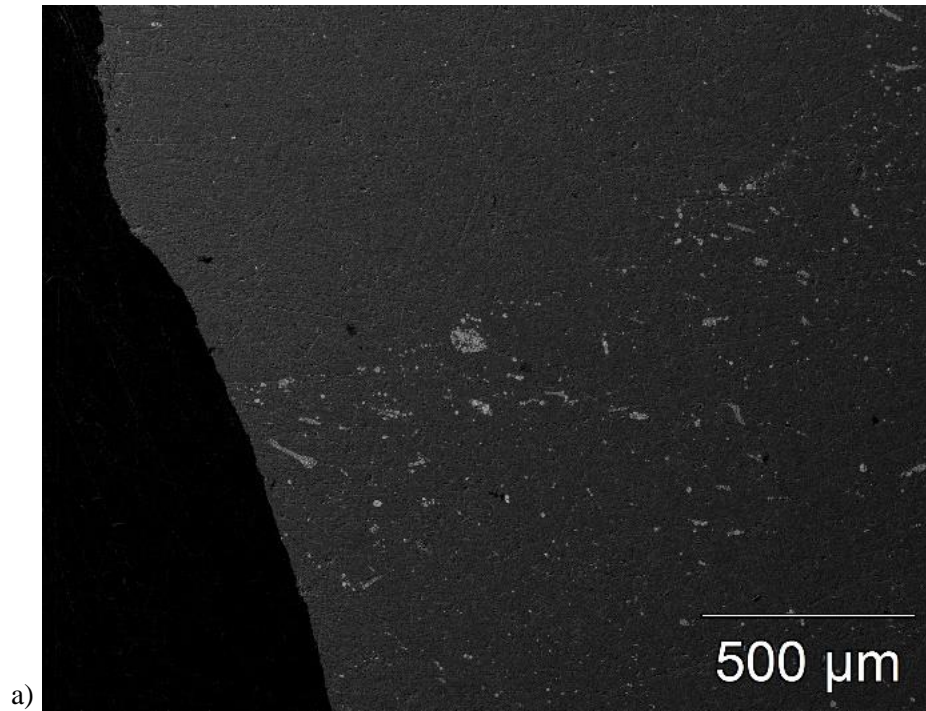
amphiboles and organic-rich clasts (Fig. 8).

Figure 4: Two SEM images of sample 31RCCW; a) silica matrix of 31RCCW. Two zones were present: one containing no pyritized matter, surrounded by a ring containing the pyritized matter, and b) the calcite shell of a foraminifera, surrounded and infilled with the silica matrix.
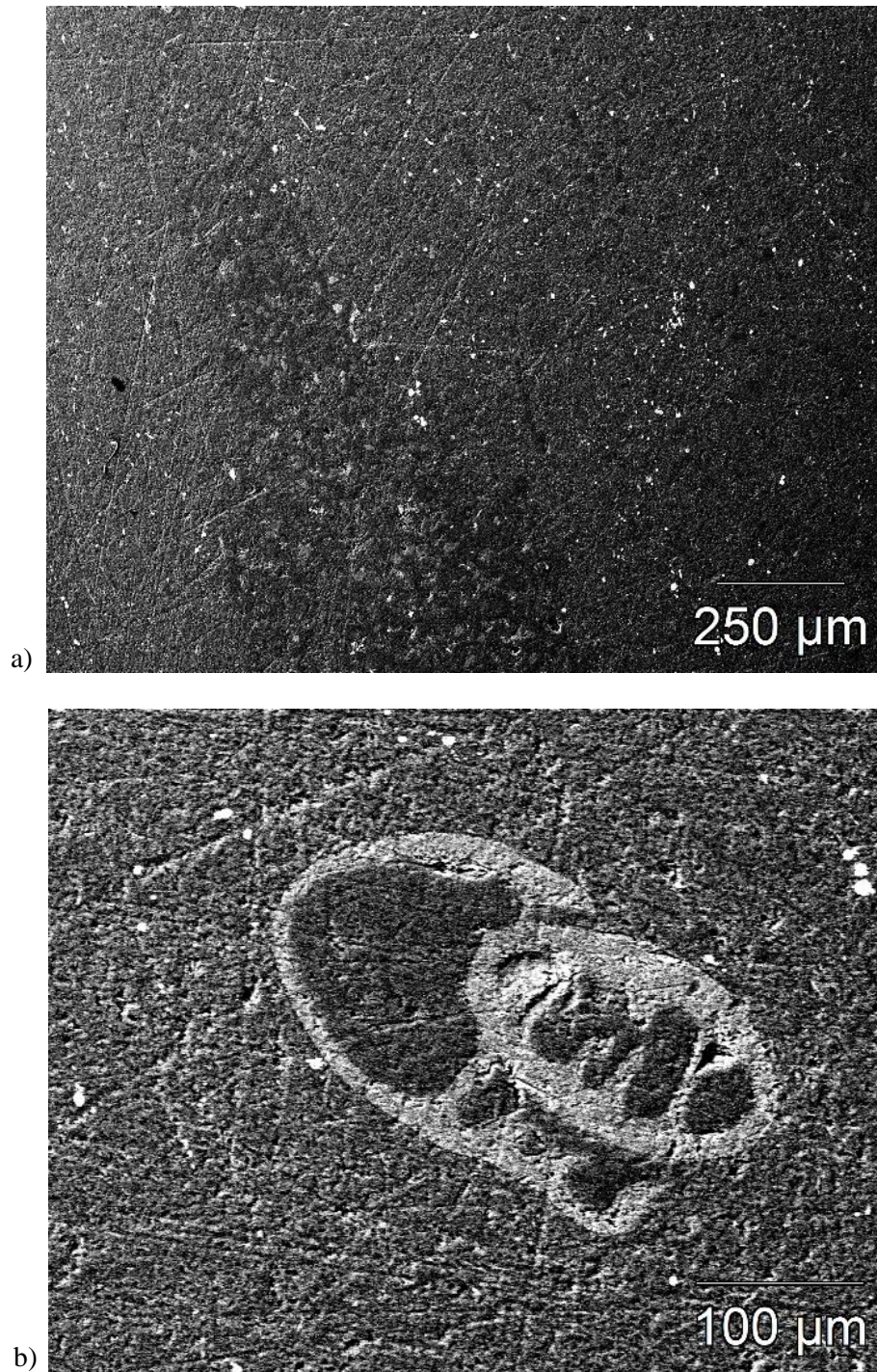
Figure 5: Images of sample 33R1W; a) bulk matrix of the sample, the white being pyritized matter, light gray silica matrix, and dark gray being Na-feldspar, and b) another calcite shell of a foraminifera, surrounded and infilled with the silica matrix.
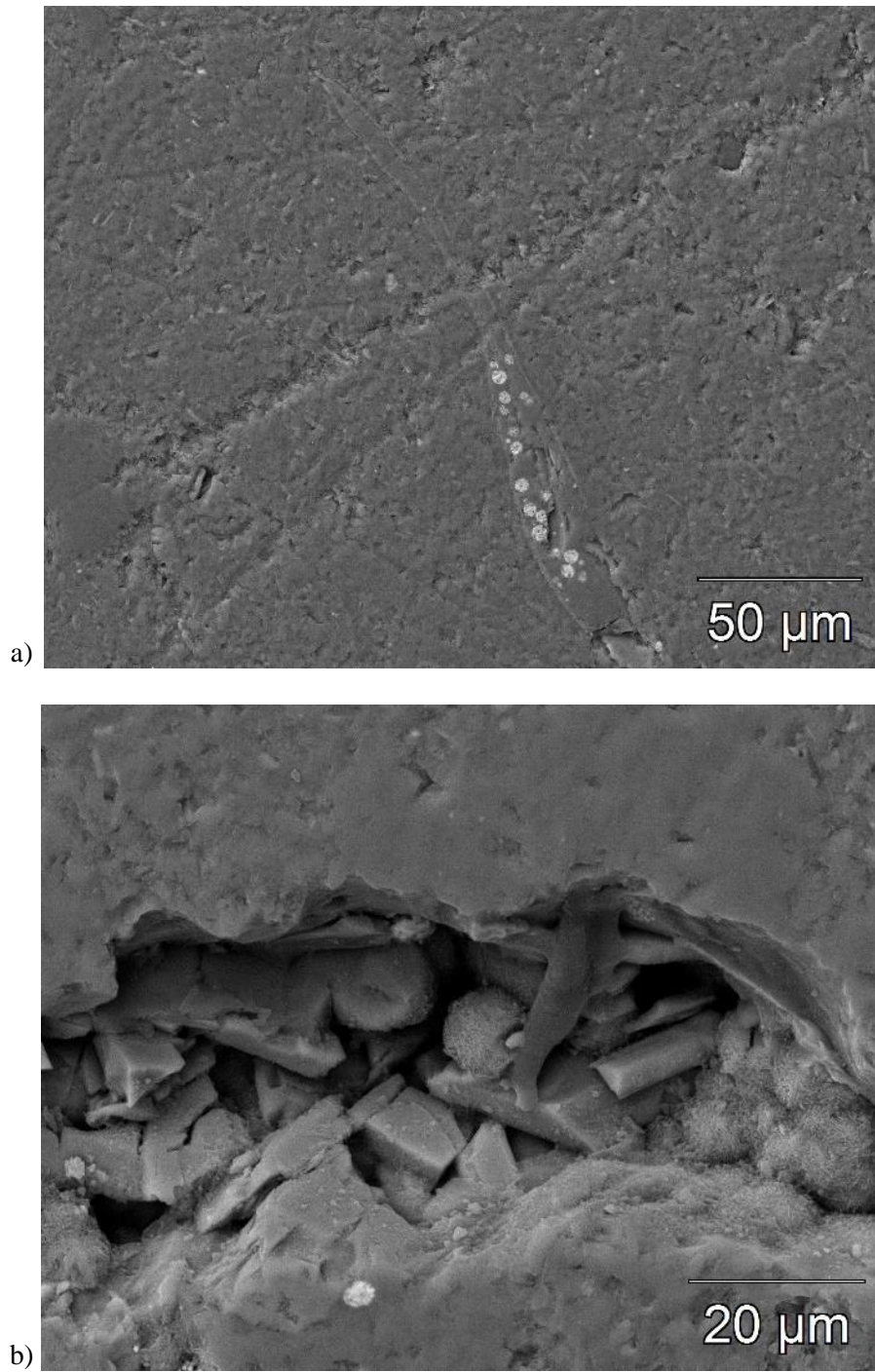
Figure 6: Images of sample 34RCCW; a) cross section of a containing pyritized organic matter in the silica matrix, and b) magnified section of the above image showing calcite crystals (blades) and probably opal-CT (spheres).
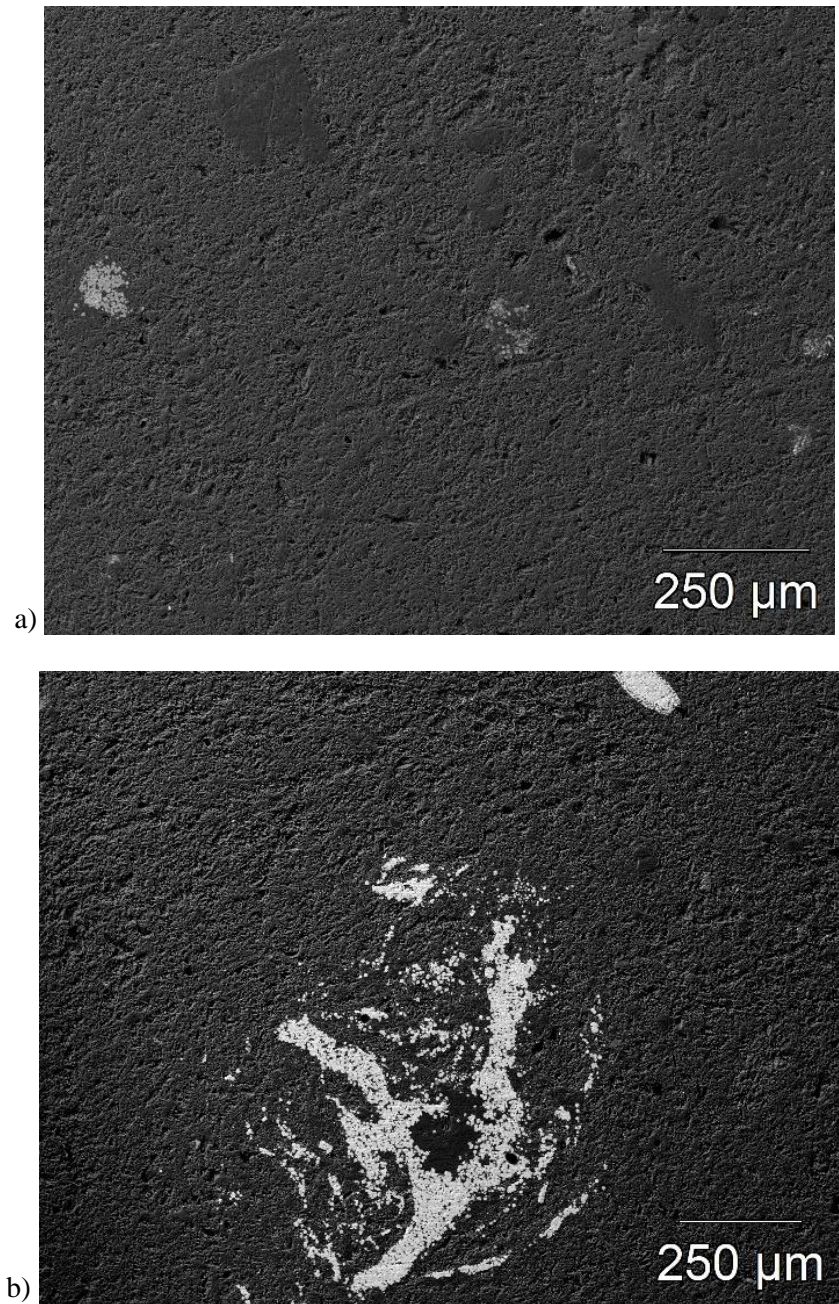
Figure 7: Two SEM images of sample 36R1W; a) the medium gray carbonate matrix dominating the sample, the darker gray are feldspars (primarily Na and Ca feldspars), and the light gray being pyritized matter, and b) large grouping of pyritized matter, including a complete diatom in the upper right.
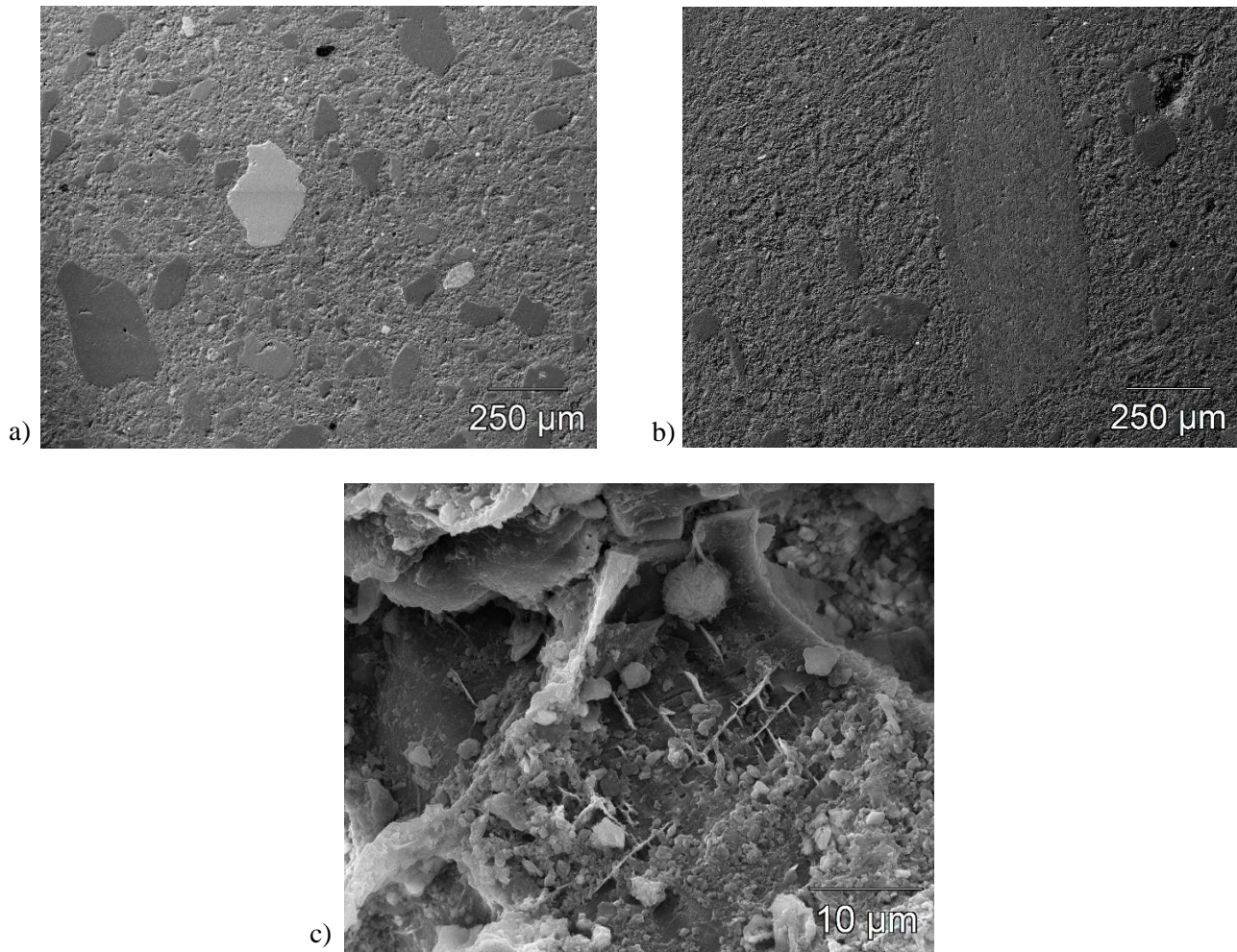
Figure 8: Images from samples taken from 37R2W: a) image of 37R2W 15/17, containing the medium gray carbonate matrix, the light gray Na feldspars, and the dark gray K-feldspars, b) image of 37R2W 65/67, containing the matrix and clasts of the same composition as 37R2W 15/17, and c) a magnified area from 37R2W 65/67, containing the carbonate matrix, opal-CT spheres, and a calcite cement.

In the chert samples, SiO_2 content decreased with depth (i.e., down core), while Al_2O_3, CaO, MgO, and MnO content increased to varying degrees between the two types of samples. Samples 31RCCW, 33R1W, and 34RCCW each had a very high SiO_2 content, ranging 92 wt. % to 84 wt. % in 31RCCW and 34RCCW respectively. The down core increase in CaO, MgO, and MnO was small in these samples, with increasing the most relative to SiO_2. FeO and K_2O all followed a similar, but weaker trend to Al_2O_3. The complete data is listed in Tables 1, 2, and 3 in the Appendix.

Samples 36R1W, 37R2W 15/17, and 37R2W 65/67, were all determined to have carbonate matrices, with a significant increase in CaO, MgO, and MnO content compared to the three upper samples. The matrix in 36R1W specifically contained higher MgO wt. % than the other two, which were higher in CaO. SiO_2 content was lowest in these samples, as was the case with FeO, K_2O, and Al_2O_3. The complete data for these samples is listed in Tables 4, 5, and 6 in the Appendix.

All data was calibrated using SiO_2 as an internal standard, excluding the data from 36R1W, which used MgO. This was done to correct quantification errors producing over 100 wt. % values of several elements in 36R1W. Additionally, the calibration for the remaining two carbonate samples (37R2W 15/17 and 37R2W 65/67) was not well-constrained, as a result of carbonate calibration difficulties. The data assumes all Ca and Mg are associated with their respective oxide, which is unlikely based on EDS analysis. As a result, the data collected regarding those two samples serves more as a qualitative measure than quantitative.

Discussion

EDS and ICP-MS data both revealed different trends regarding the compositions of the samples; EDS provided a broader view of the bulk composition (e.g., silicate or carbonate), while the ICP-MS provided a more precise analysis of the matrix. Both demonstrate a difference in bulk matrix composition between samples. 31RCCW, 33R1W, and 34RCCW were significantly higher in silica than the remaining three, while samples 36R1W, 37R2W 15/17, and 37R2W 65/67 all had a higher carbonate content. Both confirmed the initial chert and diamictite lithologies presented in McKay et al. (2019).

The more specific elemental analysis from the ICP-MS, however, further divided the chert and diamictite samples. The chert samples decreased in silica content down-core but increased in clay minerals. In the three diamictite samples, 36R1W had a more dolomitic matrix compared to the two taken from 37R2W, while 37R2W 15/17 had a higher silica content than 37R2W 65/67, both suggesting a transitory period between the shift from silicate to carbonate depositional environments (Fig. 9). The transition may have been the result of a change in the carbonate compensation depth, caused by warming and shallowing of waters down-core, or basin over-deepening with glacial advance.

The strong correlation between silica content and CaO, MgO, and MnO seen in the ICP-MS data shows near perfect-end member mixing of the silicate, carbonate, and transition groups, with the transition period being more variable than the other two (Fig. 10; Fig 12a). The relation between SiO_2 and MgO was the strongest (R^2: >60% SiO_2 = 0.92, <60% SiO_2 = 0.99), followed by SiO_2 and CaO (R^2: >60% SiO_2 = 0.80, <60% SiO_2 = 0.99), and SiO_2 and MnO (R^2: >60% SiO_2 = 0.79, <60% SiO_2 = 0.93). CaO, MgO, and MnO increase with depth down-core and display a strong end-member mixing relationship. The two groups, silicates and carbonates, each have samples that represent a matrix containing a majority of SiO_2 or carbonates. As the

boundary between the two is approached, the composition changes to reflect the differing deposition, in some cases mixing the two. This results in the relationship seen in Fig. 10; a group of ~80 wt. % carbonates and <15 wt. % SiO_2, a group of <15 wt. % carbonates and ~70 wt. % SiO_2, and a third group of ~50 wt. % carbonates and ~40 wt. % SiO_2. The changes in carbonate content in the samples is likely derived from a change in the depositional environment and carbonate compensation depth, as stated earlier.

There is a similar trend between silica content and Al_2O_3, FeO, and K_2O in the same groupings as the CaO, MgO, and MnO trends. There is a group of high SiO_2 and low elemental oxide, a group of low SiO_2 and relatively high elemental oxide, and a more variable group seeming to be a combination of the two between them. The most notable of the relationships is that between SiO_2 and Al_2O_3 (R^2: >60% SiO_2 = 0.96, <60% SiO_2 = 0.93), which also displayed a close-to-normal distribution (Fig. 11; Fig 12b). The relationship between SiO_2 and FeO display a similar but weaker trend to Al_2O_3 (R^2: >60% SiO_2 = 0.83, <60% SiO_2 = 0.72), as do SiO_2 and K_2O (R^2: >60% SiO_2 = 0.67, <60% SiO_2 = 0.90). The relations mirror that of the CaO, MgO, and MnO; that is, there is one end member that is high in silica and relatively low in the oxide, a group that is low in silica and relatively high in the oxide, and a group between the two as they mix approaching the boundary between members.

However, unlike the silica and carbonate relationships, the silica and other oxides— mostly belonging to clay minerals such as illite and chlorite—have a significantly more variable relation, particularly in the high silica range. In ~70 wt. % SiO_2 end member of the carbonate relations, the major carbonate elements, Ca and Mg, only change ~4 wt. %. Comparatively, the variability of the major oxide, Al_2O_3, varies by ~12 wt. % over the same range in SiO_2 content. The low silica range (<15 wt. % SiO_2) and the other oxides were less variable, varying less than

~10% of the total wt. % difference of each. The grouping around ~40% SiO_2 with the other

oxides had a similar variability compared to the middle carbonate grouping. The changes in

Al_2O_3, FeO, and K_2O are likely a result of increase in the incorporation of the clay minerals from

more heavily weathered material, particularly in the chert samples which maintained a

microcrystalline matrix throughout, while it may also be attributed to the incorporation of larger
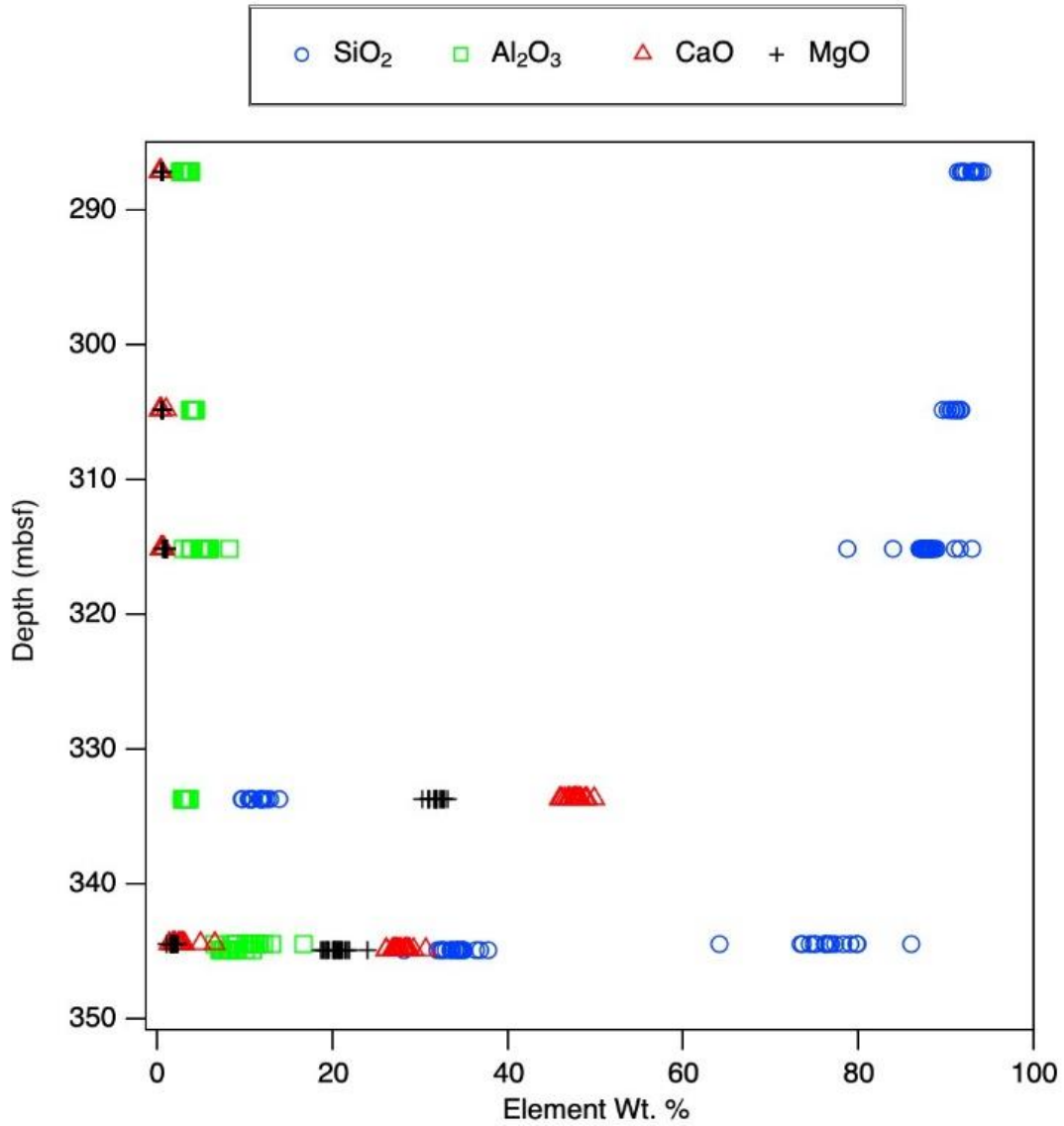
silicate clasts in the diamictite samples.

Figure 9: Elemental wt. % changes with depth (mbsf) for SiO_2, Al_2O_3, CaO, and MgO created

from ICP-MS data. The second of the diamictite samples, 37R2W 15/17, has an elevated SiO_2

content compared to the two other diamictite samples, likely due to higher clast density.
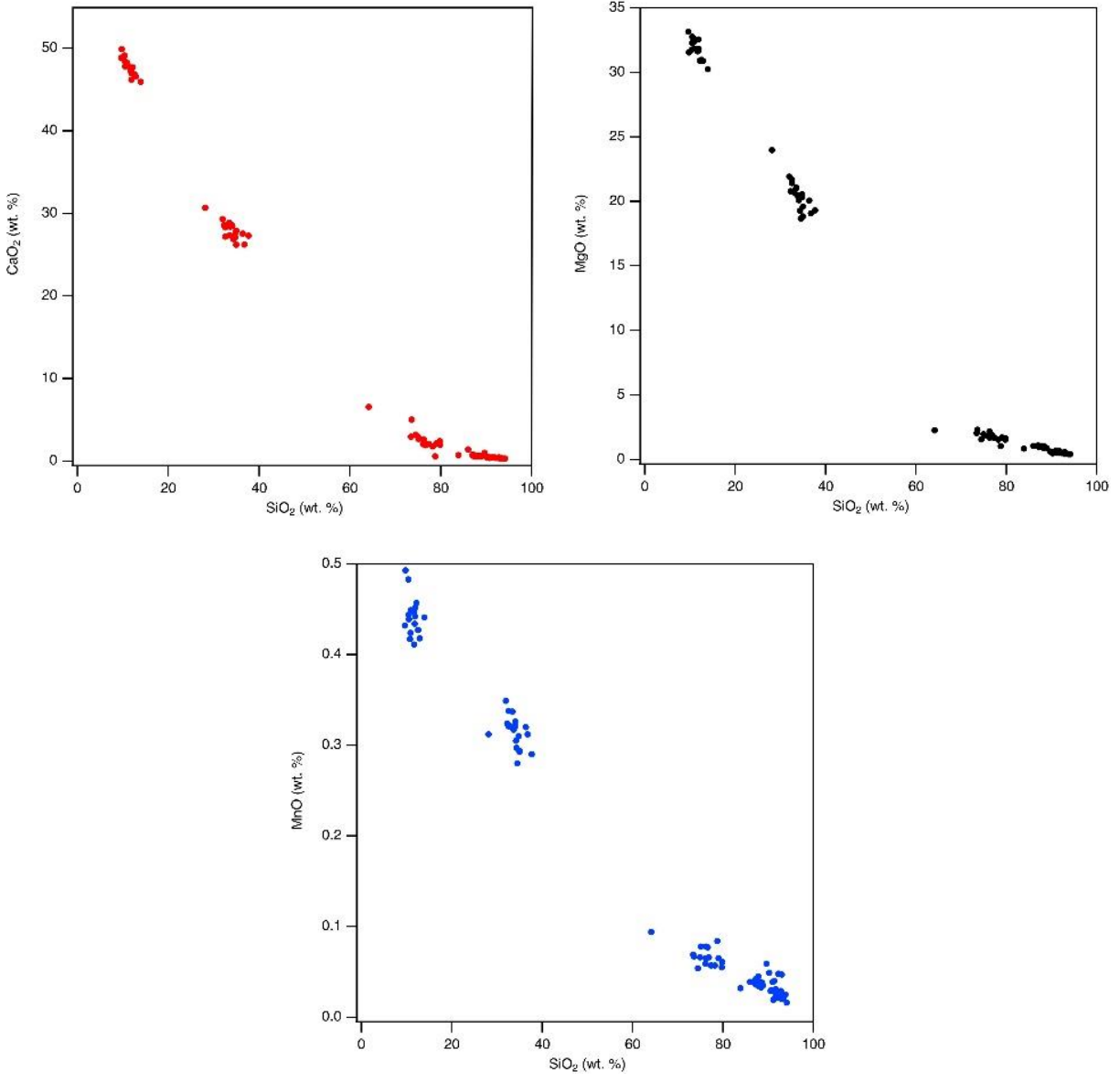
Figure 10: Three plots comparing the wt. % values of CaO (red), MgO (black), and MnO (blue) to SiO_2 wt. %. Three distinct groups are seen: 1) high SiO_2 and lower CaO/MgO/MnO, 2) low SiO_2 and higher CaO/MgO/MnO, and 3) an intermediate rock between the two.
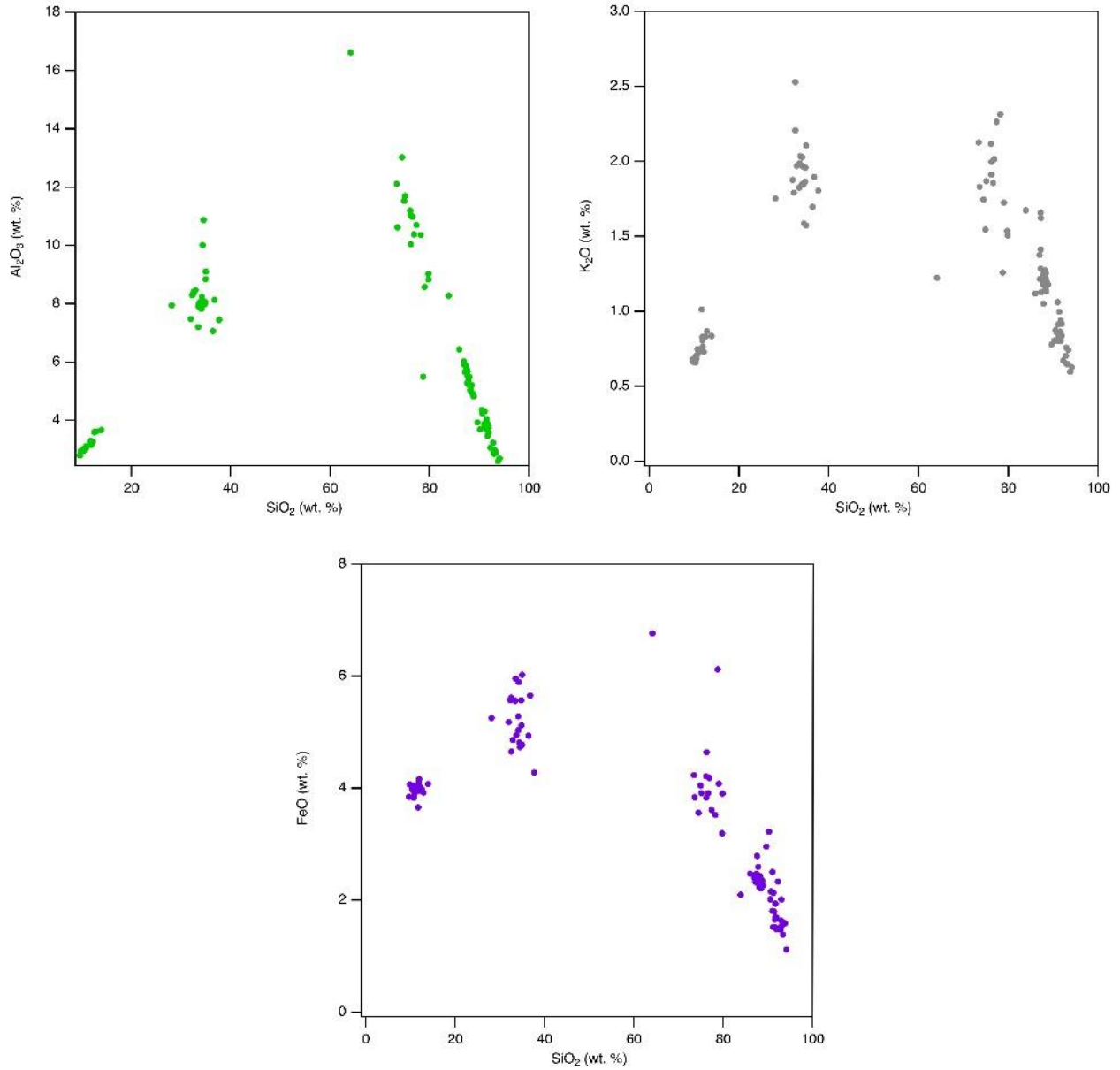
Figure 11: Three plots comparing the wt. % values of Al (green), Fe (purple), and K (gray) to SiO$_2$ wt. %. Three distinct groups are seen: high SiO$_2$ and a low to high spread of each, low SiO$_2$ and low wt. % of each, and a group between the two with higher variability.
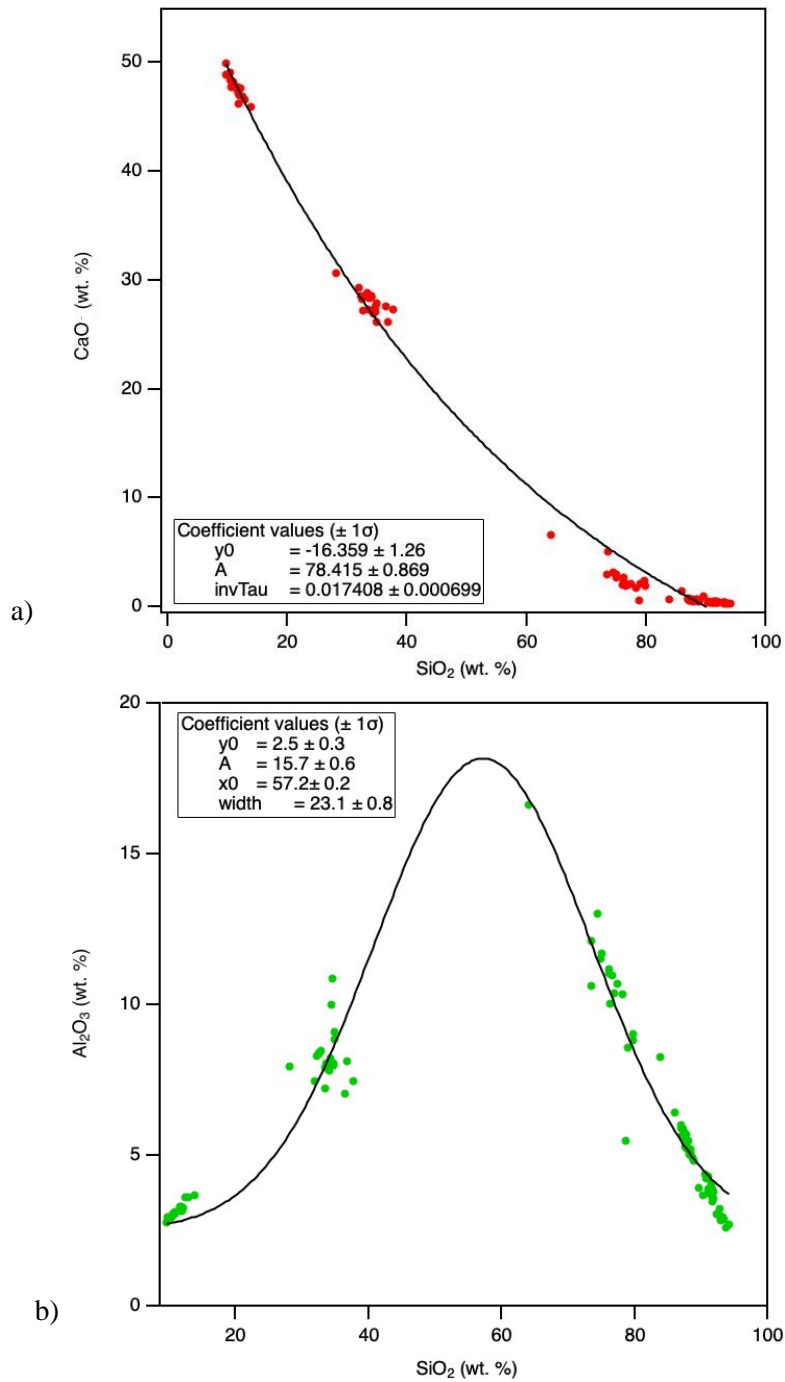
Figure 12: Two plots of data from Figures 10 and 11, demonstrating the two different

relationships: a) a plot comparing wt. % of SiO_2 and CaO, fit to an exponential curve where A is

the amplitude of the curve, and b) a plot comparing Al_2O_3 and SiO_2 wt. %, fit to a Gaussian

curve, where A is the amplitude.

Marschalek et al. (2021) present this change in depositional environment as part of the transition and start of a marine-based West Antarctic Ice Sheet just prior to the MCO. The East and West Antarctic Ice Sheets have differing geologic histories, resulting in different compositions of eroded sediments. Through geochemical, mineralogical, and petrological analysis, the origin of the sediments in Subunits VIB and VIC was determined to be in West Antarctica, while those of Subunit VIA originated from the Transantarctic Mountains in the East Antarctic, though the upper portions of Subunit VIA appear to have originated closer to the coast than the lower sections (Fig.13).

The clay minerals and other silicate clasts found in this study all point to a terrestrial origin; illite is a weathering product of muscovite, chlorite can originate from olivine, pyroxene, and hornblende, and the feldspar and quartz clasts in the diamictites seem to have been deposited in a fashion that allowed for the carbonate matrix to form around them. The clasts are only a major component in the diamictites and disappear by the top of the chert interval, becoming the heavily weathered clay minerals present. The more detrital nature of the diamictites in Unit VI most likely represents an ice-proximal to subglacial glaciomarine environment near the ice-sheet margin, while the chert nodules in Unit V likely represent the change to what was originally an ice-distal marine environment in deeper waters further from the margin. Both environments are in agreement with initial observations by McKay et al. (2019) and further support the evidence presented in Marschalek et al. (2021).

The evidence of transitioning environments supports the possibility of a marine-based West Antarctic Ice Sheet during cooler temperatures just prior to the MCO, which then retreated when average global temperatures increased. This retreat, reflected in Subunit VIA and Unit V by their respective compositions, has been proposed to have been the tipping point of the West

Antarctic Ice Sheet's shift from a primarily terrestrial ice sheet to a marine-based ice sheet (Marschalek et al., 2021). The marine ice sheet, with significant ice masses exposed to warming ocean waters, would then be more susceptible to changes in heat and environment, as is seen presently, and would be responsible for the far-field sea level rise seen at the time. This then indicates the East Antarctic Ice Sheet retained most of its ice mass through the MCO, suggesting that substantial portions of the East Antarctic Ice Sheet may remain at future elevated global temperatures when compared to pre-Industrial temperatures.
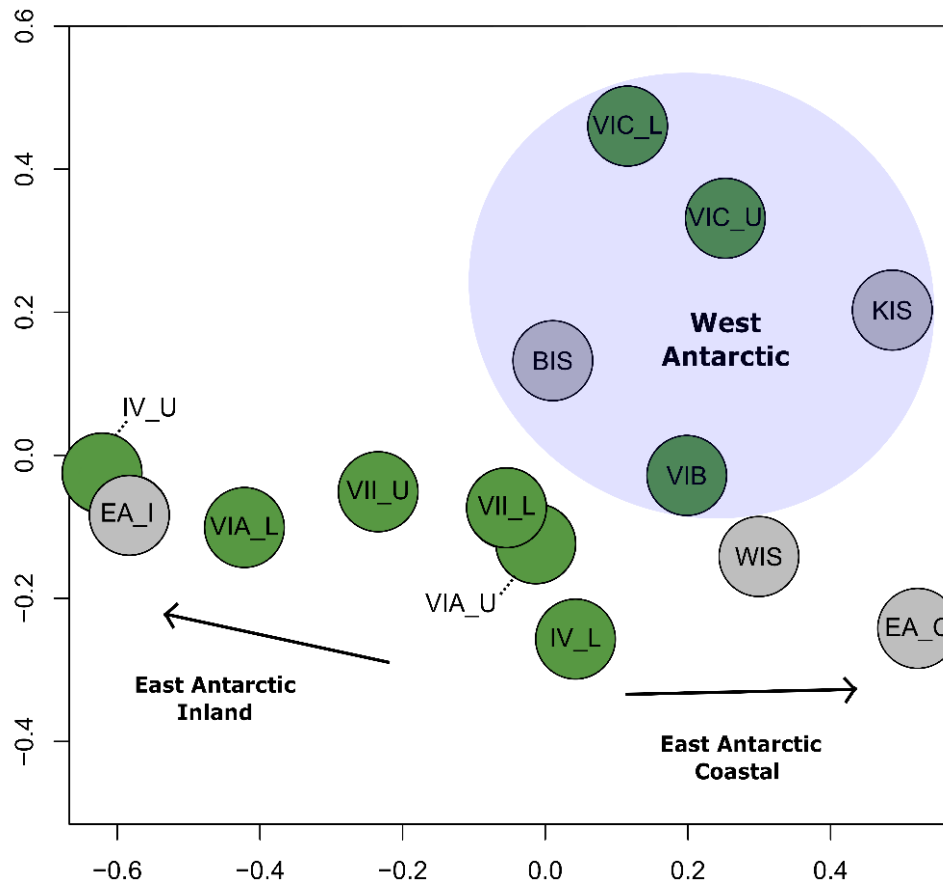
Figure 13: A multi-dimensional scaling plot of zircon U-Pb age kernel density estimates calculated with Kolmogorov-Smirnov statistics. Samples from IODP Site U1521 are in green and are compared to previously published zircon U-Pb ages (gray) of the Whillans (WIS), Kamb (KIS), and Bindschadler (BIS) ice streams, and inland and coastal moraine regions of the Transantarctic Mountains (EA_I and EA_C, respectively). Those interpreted to have originated in from the West Antarctic fall in the area shaded in blue (adapted from Marschalek et al., 2021).

Conclusions

Differences in composition between the chert and diamictite lithologies, presented as an end-member mixing relationship between carbonate and silicate members, represent a transition of depositional environment during the early Miocene. The older, carbonate-rich diamictites in Unit VI reflect an ice-proximal to subglacial environment, while the silica-rich chert nodules of Unit V represent a diagenetically altered ice-distal environment. This shift in environmental origin, combined with the East Antarctic provenance of sediments in Subunit VIA and the West Antarctic provenance of Subunits VIB and VIC, suggest a retreat of the West Antarctic Ice Sheet at the onset of the MCO and resulting in the far-field sea level rise seen in sedimentological records of the time. The exact timing of this event remains poorly constrained but may represent a turning point for the West Antarctic Ice Sheet's transition to a marine-based ice sheet. That transition made the West Antarctic Ice Sheet more sensitive to changes in global climate, influencing the Antarctic response to warmer global temperatures during the MCO. The increased sensitivity of the marine-based ice sheet means that, while the East Antarctic Ice Sheet may not see the same ice-mass loss as the West Antarctic Ice Sheet, the current trend of warming global temperatures as a result of anthropogenic climate change does pose a risk to the West Antarctic Ice Sheet and the water volume within it.

Acknowledgements

References

Anderson, J.B., Simkins, L.M., Bart, P.J., De Santis, L., Halberstadt, A.R.W., Olivo, E., and
Greenwood, S.L. (2018) Seismic and geomorphic records of Antarctic Ice Sheet
evolution in the Ross Sea and controlling factors in its behaviour. Glaciated Margins: The
Sedimentary and Geophysical Archive, Geological Society Special Publication. 475.
https://doi.org/10.1144/SP475.5

Barrett, P.J. (1981) History of the Ross Sea region during the deposition of the Beacon
Supergroup 400–180 million years ago. Journal of the Royal Society of New Zealand.
11:4, 447–458.

Bart, P.J. (2003) Were West Antarctic Ice Sheet grounding events in the Ross Sea a consequence
of East Antarctic Ice Sheet expansion during the middle Miocene. Earth and Planetary
Science Letters. 216 (1–2), 93–107. https://doi.org/10.1016/S0012-821X(03)00509-0

Behrendt, J.C., LeMasurier, W.E., Cooper, A.K., Tessensohn, F., Tréhu, A., and Damaske, D.
(1991) Geophysical studies of the West Antarctic rift system. Tectonics. 10:6, 1257–
1273. https://doi.org/10.1029/91TC00868

Cooper, A.K., Barrett, P.J., Hinz, K., Traube, V., Leitchenkov, G., and Stagg, H.M.J. (1991)
Cenozoic prograding sequences of the Antarctic continental margin: a record of glacio-
eustatic and tectonic events. Marine Geology. 102:1–4, 175–213.
https://doi.org/10.1016/0025-3227(91)90008-R

De Santis, L., Anderson, J.B., Brancolini, G., and Zayatz, I. (1995) Seismic record of late
Oligocene through Miocene glaciation on the Central and Eastern Continental Shelf of
the Ross Sea. Antarctic Research Series. 68: Geology and Seismic Stratigraphy of the

Antarctic Margin: Washington, DC (American Geophysical Union), 235–260.

https://doi.org/10.1029/AR068p0235

Foster, G.L., and Rohling, E.J. (2013) Relationship between sea level and climate forcing by

CO2 on geological timescales. Proceedings of the National Academy of Sciences. 110:4,

1209–1214. https://doi.org/10.1073/pnas.1216073110

IPCC (2021) Summary for Policy Makers, *in* Masson-Delmotte, V., Zhai, P., Pirani, A.,

Connors, S. L., Péan, C., Berger, S., Caud, N., Chen, Y., Goldfarb, L., Gomis, M.I.,

Huang, M., Leitzell, K., Lonnoy, E., Matthews, J.B.R., Maycock, T.K., Waterfield, T.,

Yelekçi, O., Yu, R., and Zhou, B., eds., Climate Change 2021: The Physical Science

Basis. Contribution of Working Group I to the Sixth Assessment Report of the

Intergovernmental Panel on Climate Change. Cambridge University Press. 6, 4-36.

John, C.M., Karner, G.D., Browning, E., Leckie, R.M., Mateo, Z., Carson, B., and Lowery, C.

(2011) Timing and magnitude of Miocene eustasy derived from the mixed siliciclastic-

carbonate stratigraphic record of the northeastern Australian margin. Earth and Planetary

Science Letters. 304:3–4, 455–467. https://doi.org/10.1016/j.epsl.2011.02.013

Kominz, M.A., Browning, J.V., Miller, K.G., Sugarman, P.J., Misintseva, S., and Scotese, C.R.

(2008) Late Cretaceous to Miocene sea-level estimates from the New Jersey and

Delaware coastal plain coreholes: an error analysis. Basin Research. 20:2, 211–226.

https://doi.org/10.1111/j.1365-2117.2008.00354.x

Kominz, M.A., Miller, K.G., Browning, J.V., Katz, M.E., and Mountain, G.S. (2016) Miocene

relative sea level on the New Jersey shallow continental shelf and coastal plain derived

from one-dimensional backstripping: A case for both eustasy and epeirogeny. Geosphere.

12:5. https://doi.org/10.1130/GES01241.1

Kopp, R.E., Simons, F.J., Mitrovica, J.X., Maloof, A.C., and Oppenheimer, M. (2009) Probabilistic assessment of sea level during the last interglacial stage. Nature. 462:7275, 863–867. https://doi.org/10.1038/nature08686

Levy, R., Harwood, D., Florindo, F., Sangiorgi, F., Tripati, R., von Eynatten, H., Gasson, E., et al. (2016) Antarctic Ice Sheet sensitivity to atmospheric CO_2 variations in the early to mid-Miocene. Proceedings of the National Academy of Sciences of the United States of America. 113:13, 3453–3458. https://doi.org/10.1073/pnas.1516030113

McKay, R., Naish, T., Carter, L., Riesselman, C., Dunbar, R., Sjunneskog, C., Winter, D., et al. (2012) Antarctic and Southern Ocean influences on late Pliocene global cooling. Proceedings of the National Academy of Sciences of the United States of America. 109:17, 6423–6428. https://doi.org/10.1073/pnas.1112248109

McKay, R.M., De Santis, L., Kulhanek, D.K., et al. (2019). Expedition 374 summary. Proceedings of the International Ocean Discovery Program. 374. https://doi.org/10.14379/iodp.374.101.20192

Miller, K.G., Kominz, M.A., Browning, J.V., Wright, J.D., Mountain, G.S., Katz, M.E., Sugarman, P.J., Cramer, B.S., Christie-Blick, N., and Pekar, S.F., 2005. The Phanerozoic record of global sea-level change. Science. 310:5752, 1293–1298. https://doi.org/10.1126/science.1116412

Miller, K.G., Wright, J.D., Browning, J.V., Kulpecz, A., Kominz, M., Naish, T.R., Cramer, B.S., Rosenthal, Y., Peltier, W.R., and Sosdian, S. (2012) High tide of the warm Pliocene: implications of global sea level for Antarctic deglaciation. Geology. 40:5, 407–410. https://doi.org/10.1130/G32869.1

Miller, K.G., Browning, J.V., Schemlz, J.W., Kopp, R.E., Mountain, G.S., and Wright, J.D.

(2020) Cenozoic sea-level and cryospheric evolution from deep-sea geochemical and continental margin records. Science Advances. 6. https://doi.org/10.1126/sciadv.aaz1346

Naish, T.R., Powell, R., Levy, R., Wilson, G., Scherer, R., Talarico, F., Krissek, L., et al. (2009) Obliquity-paced Pliocene West Antarctic Ice Sheet oscillations. Nature. 458:7236, 322–329. https://doi.org/10.1038/nature07867

Naish, T.R., and Wilson, G.S. (2009) Constraints on the amplitude of mid-Pliocene (3.6–2.4 Ma) eustatic sea-level fluctuations from the New Zealand shallow-marine sediment record. Philosophical Transactions of the Royal Society, A: Mathematical, Physical & Engineering Sciences. 367:1886, 169–187. https://doi.org/10.1098/rsta.2008.0223

Naish, T.R., Woolfe, K.J., Barrett, P.J., Wilson, G.S., Atkins, C., Bohaty, S.M., Bücker, C.J., et al. (2001) Orbitally induced oscillations in the East Antarctic Ice Sheet at the Oligocene/Miocene boundary. Nature. 413:6857, 719–723. https://doi.org/10.1038/35099534

Pagani, M., Zachos, J.C., Freeman, K.H., Tipple, B., and Bohaty, S. (2005) Marked decline in atmospheric carbon dioxide concentrations during the Paleogene. Science. 309:5734, 600–603. https://doi.org/10.1126/science.1110063

Passchier, S., Browne, G., Field, B., Fielding, C.R., Krissek, L.A., Panter, K., Pekar, S.F., and ANDRILL-SMS Science Team (2011) Early and middle Miocene Antarctic glacial history from the sedimentary facies distribution in the AND-2A drill hole, Ross Sea, Antarctica. Geological Society of America Bulletin. 123:11–12, 2352–2365. https://doi.org/10.1130/B30334.1

Pekar, S.F. and DeConto, R.M. (2006) High resolution ice-volume estimates for the early

Miocene: Evidence for a dynamic ice sheet in Antarctica. Paleogeography, Paleoclimatology, Paleoecology. 231, 101–109. https://doi.org/10.1016/j.palaeo.2005.07.027

Scherer, R.P., Aldahan, A., Tulaczyk, S., Possnert, G., Engelhardt, H., and Kamb, B. (1998.) Pleistocene collapse of the West Antarctic Ice Sheet. Science. 281:5373, 82–85. https://doi.org/10.1126/science.281.5373.82

Shevenell, A.E., Kennett, J.P., and Lea, D.W. (2004) Middle Miocene Southern Ocean cooling and Antarctic cryosphere expansion. Science. 305:5691, 1766–1770. https://doi.org/10.1126/science.1100061

Shevenell, A.E., Kennett, J.P., and Lea, D.W. (2008) Middle Miocene ice sheet dynamics, deep-sea temperatures, and carbon cycling: a Southern Ocean perspective. Geochemistry, Geophysics, Geosystems. 9:2. https://doi.org/10.1029/2007GC001736

Siddoway, C.S., Baldwin, S.L., Fitzgerald, P.G., Fanning, C.M., and Luyendyk, B.P. (2004) Ross Sea mylonites and the timing of intracontinental extension within the West Antarctic rift system. Geology. 32:1, 57–60. https://doi.org/10.1130/G20005.1

Ten Brink, U.S., Schneider, C., and Johnson, A.H. (1995) Morphology and stratal geometry of the Antarctic continental shelf: insights from models. Antarctic Research Series. Volume 68): Geology and Seismic Stratigraphy of the Antarctic Margin: Washington, DC (American Geophysical Union), 1–24. https://doi.org/10.1029/AR068p0001